RSC Advances

ROYAL SOCIETY OF CHEMISTRY

www.rsc.org/advances

Journal Name

ARTICLE

The Non-Innocent Nature of Graphene Oxide as Theranostic Platform for Biomedical Applications and its Reactivity towards Metal-Based Anticancer Drugs

Received 00th January 20xx,
Accepted 00th January 20xx

DOI: 10.1039/x0xx00000x

www.rsc.org/

Audrey Mokdad,[a*] Konstantinos Dimos,[b] Giorgio Zoppellaro,[a*] Jiri Tucek,[a] Jason A. Perman,[a] Ondrej Malina,[a] K. Kristoffer Andersson,[c] Kasibhatta Kumara Ramanatha Datta,[a] Jens Peter Froning[a] and Radek Zboril[a*]

The self-assembly process in solution of a mononuclear iron (II) complex based on the bispyrazolylpyridine scaffold with graphene oxide (GO) micrometer-sheets allows devising not only a new hybrid-architecture for GO-based materials suitable for nanomedicine, but also unveiling the reactive nature of GO as drug-carrier. The neat iron complex is found highly active in disrupting cell's cycle through DNA binding, with behaviour and efficiency similar to that expressed by Ruthenium-complexes as well as antibiotic-drugs such as doxorubicin. On the contrary, in the hybrid material the proclivity of neat GO to produce reactive oxygen species (ROS) became down-regulated by the electron-buffering properties of the loaded iron complex, evidencing the presence of an active electron transfer from the drug to GO. These findings question the use of the neat GO platform as suitable carrier for metal-based anticancer drugs and highlight the importance of addressing the chemical/physical integrity of the drug being loaded into GO before drawing conclusions on the potential effectiveness of the hybrid material for medical applications.

Introduction

The synthesis of functional nanomaterials based on graphene-oxide (GO) nano/micrometer sheets suitable for drug delivery, biosensing and imaging represent nowadays a vast ground of research in medical nanotechnology.[1] Being water dispersible, GO offers an organic scaffold that is prone to be used in biological environments. Several derivatives of GO have been prepared that aid the delivery of, for example, anticancer drugs (e.g. doxorubicin, camptothecin),[2] genes (siRNA) and antibodies,[3] they can form antithrombogenic materials (e.g. GO based heparin mimicking hydrogels),[4] can act or aid delivery of fluorescent probes for bio-imaging,[5] biosensors[6] and can form substrates for implants and tissue engineering.[7] Despite the breath of applications and the body of work produced in literature on GO-based materials, the biosafety of GO remains still under extensive revision.[1] GO is capable to express toxicity and genotoxicity against a variety of cell's type (e.g. erythrocytes, fibroblasts, lung carcinoma, mesenchymal stem cells) and has shown proclivity to induce alterations in the mitochondrial activity and severe oxidative stress through generation of reactive oxygen species (ROS), both to plasma membranes and nuclear DNA.[8] Several different synthetic strategies have been explored in a way to minimize/reduce the cytotoxicity of GO; for example, through the introduction of PEG chains in the GO-sheets or upon decreasing the dimension of the GO sheets, down to the nm-range (nGO).[9] It has been recognized that the toxicity of GO is strongly augmented by the presence of small amounts of metal contaminants (e.g. manganese cations from potassium permaganate) used as oxidant source for the GO synthesis. The presence of such impurities trapped in the GO layers has generated a range of diverse concentrations in which cytotoxic behaviour of GO starts to emerge.[8] However, even when such contaminants are carefully removed from the material, the presence structural defects typical for GO, the system's charge, the sheet sizes, degree of aggregation and oxidation are all factors capable to trigger the cytotoxicity and/or ROS response when cells are exposed to GO.[8,10] In spite of these limitations and the number of questions left open about the metabolism of GO at cellular level, its use for biomedical applications remains for the scientific community much promising, especially in the

[a] Regional Centre of Advanced Technologies and Materials, Slechtitelu 27, 78371 Olomouc, Czech Republic
E-mail: giorgio.zoppellaro@upol.cz; radek.zboril@upol.cz; audrey.mokdad@upol.cz
[b] Department of Materials Science & Engineering, University of Ioannina, GR-45110 Ioannina, Greece
[c] Department of Biosciences (IBV), University of Oslo, NO-0371 Oslo, Norway
†Electronic Supplementary Information (ESI) available: DTA/TG/DTG curves, additional XPS data, SEM and TEM micrographs, additional Mössbauer data, FT-IR, Raman, UV-Vis, fluorescence spectra, binding spectra and plot-analysis, additional cytotoxicity test on NIH3T3 cells of Fe-Pz_2Py, and DFT calculations (including input files). See DOI: 10.1039/x0xx00000x

construction of novel delivery systems for anticancer drugs.[1,11] Anticancer drugs represent one of the key components in the modern pharmacotherapies and are widely used against various forms of neoplasia. They act in a way to disrupt specific stages of the cell's cycle, impacting cell's survivals and/or proliferation.[12] Anticancer drugs express their toxicity, for example, through direct binding of the DNA base-pair as featured by organometallic complexes such as cisplatin (Pt-*cis*, *cis*-diamminedichloroplatinium(II)) and Pt-derivatives, or *via* DNA intercalation and/or ROS generation as witnessed in general for ruthenium-based complexes[13-18] and antibiotic-based drugs such as doxorubicin (DOX) and camptothecin.[19] In order to provide formulations that are safer for the effective use in medical therapies, it is essential to understand better in GO-based materials the contribution to the observed cytotoxicity of the drug from the cytotoxicity associated to GO, and to devise alternative synthetic strategies as to control/down-regulate the toxic effect brought by the latter. Most importantly, it is critical to openly address the question of the actual function of GO in drug delivery; does GO act universally as an innocent carrier, although with variable cytotoxicity, or is it capable to alter in same cases the chemical integrity and nature of the loaded drug. In this work we demonstrate that GO may not simply act as a carrier. We used for the purpose a mononuclear iron complex Fe(II)-Pz_2Py as novel cytotoxic compound for the construction of an hybrid GO system. The organometallic complex is merged with graphene oxide (GO) micro-meter sheets, by using electrostatic and π-π interactions as driving forces for the assembly process (Figure 1).

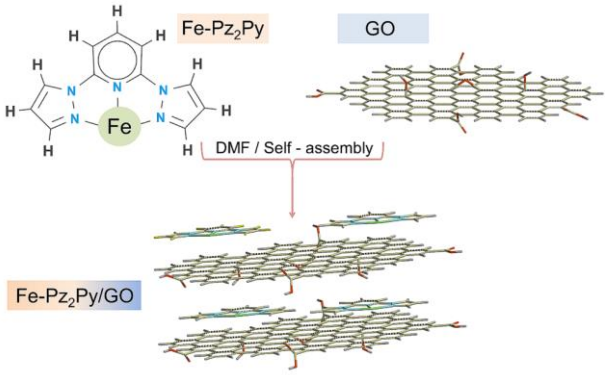

Figure 1. The self-assembly process in solution (dimethylformamide, DMF) between the mononuclear iron (II) complex (Fe-Pz_2Py) and graphene oxide (GO) with formation of the hybrid material (Fe-Pz_2Py/GO).

This procedure, which follows the non-covalent pathway for drug's loading into GO sheets, is the usual route pursued by many groups, including us, for preparing GO-based drug delivery systems.[1] We demonstrate that neat Fe(II)-Pz_2Py is a cytotoxic drug but it is also a sensitive probe, which allows monitoring the changes in the electronic fingerprint of the Fe(II)-Pz_2Py complex upon loading into GO. Although Fe(II)-Pz_2Py remains very stable in water and DMF solutions in its S = 2 state, once loaded into GO it changes its oxidation to Fe(III) as well as the spin state, to S = 5/2. Thus, GO acts as an effective electron acceptor for Fe(II)-Pz_2Py. Furthermore, the proclivity of GO to produce reactive oxygen species becomes here down-regulated by the presence of the so-oxidized complex (Fe(III)-Pz_2Py), being the hybrid material less cytotoxic and more biocompatible than neat GO. We speculate that a similar phenomenon may also emerge for other red-ox sensitive drugs upon loading into GO, such as for Ru- and Pt-compounds. This factor, unless clearly unveiled, can undermine the deeper understanding of the metabolic impact of the GO-drug conjugate, and can substantially impair further improvements in the chemical design of these carbon based materials for biomedical applications.

Results and discussion

Synthesis and physical properties of Fe-Pz_2Py. The 2,6-bis(pyrazol-1-yl)pyridine molecule (Pz_2Py) is a tridentate nitrogen-donor ligand extensively used as molecular building unit for the synthesis of magnetic materials, such as organic high spin molecules, organometallic/spin-cross over complexes, grid-like and metallacycle supramolecular assemblies.[20-26] The application of Pz_2Py and, in particular, the iron based Pz_2Py systems beyond the field of molecular magnetism and catalysis remains less explored, especially in the biomedical context of drug design.[27-30] Synthesis of the 2,6-bis(pyrazol-1-yl)pyridine molecule is readily obtained in very good yields (> 70%) by nucleophilic substitution reaction between pyrazolate anion (potassium-salt) and 2,6-dibromo-pyridine in high boiling solvents (diglyme), as reported in literature.[31,32] Then, Fe-Pz_2Py is formed simply (> 80% yield) by mixing at room temperature (12 h, nitrogen atmosphere) equimolar amounts of $FeCl_2 \times 4\ H_2O$ and Pz_2Py in THF followed by precipitation of the bright yellow ferrous complex with diethylether.[33] The mononuclear Fe-Pz_2Py system shows moderate solubility in water (~1 mg/mL). It remains, however, in aqueous environments highly stable in the ferrous form (H_2O, MeOH/H_2O admixtures), even after prolonged storage in air at ambient temperature. The structural features of Fe-Pz_2Py, with its molecule size of 1.08 nm (lateral dimension) and the planar arrangement of the pyridine-pyrazole rings, as predicted by calculation (DFT/M06/6-31G*/LanL2DZ, Figure 2a and in Supporting Material, ESI, Figure S1), may favour its DNA intercalation following cellular uptake, an effect driven by the emergence of π-π type interactions with the purine/pyrimidine bases. The DNA intercalation proclivity of Fe-Pz_2Py is confirmed experimentally from the combined analysis of cytotoxicity and DNA binding studies (*vide infra*). In this context, Fe-Pz_2Py shares some structural characteristic (rings planarity, aromaticity) with the tetracene moiety of hydroxydaunorubicin (DOX), molecule known to undergo DNA intercalation. DOX is an anthracycline antibiotic and one of the most employed drugs against a wide range of cancers such as lymphomas, leukemias, breast, pancreas and ovaries

tumors.[34-35] DOX has been used by many groups to construct hybrid drug delivery systems in combination with GO.[1] However, differing from DOX, the presence in Fe-Pz_2Py of the iron centre in which the coordination sphere is filled by weakly bound water ligands in solution, allows the potential establishment of several other types of interactions, similar to the behaviour witnessed for ruthenium and Pt-based drugs.[13-17] For example, through the metal centre, the direct coordination with pyrimidine/purine nitrogens, carbonyl oxygen atoms and the phosphate/ribose-oxygen moieties of the DNA/RNA chains can be targeted by Fe-Pz_2Py. Fe-Pz_2Py does not exhibit spin cross-over behaviour (Fig. 2b, upper trace), and its magnetic properties are fully consistent with the presence of one ferrous cation in the high-spin electronic configuration (S = 2), over the entire temperature range examined (T = 2-300 K, (emu/g) × T at 300 K = 0.0092, value that corresponds to μ_{obs} = 5.37 B.M. with g_{eff} = 2.00 at 300 K). From Figure 2b, the witnessed drop in the (emu/g)T product below 50 K is ascribable to the zero-field splitting in the energy level of the high spin Fe(II) embedded in an octahedral environment (see also in ESI, Figure S2).

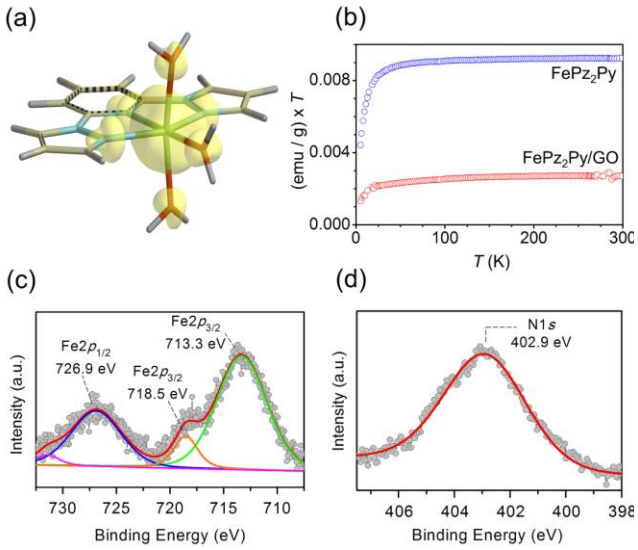

Figure 2. Panel (a) shows the geometry optimized structure of the high-spin complex Fe-Pz2Py with coordinated water molecules (3 H2O) as calculated by density functional theory (DFT, UM06/6-31G*/LanL2DZ, in vacuum). Energy = -1050.05774 a.u., charge = +2, S2 = 6.0112, ρFe = 3.77. The spin density isosurface has been drawn at 0.002 IsoValue. Panel (b) shows the temperature-dependent magnetic properties of Fe-Pz2Py (red circles) and the hybrid material Fe-Pz2Py/GO (blue circles) under 0.1 T of applied field. Panel (c) and (d) show the XPS absorption profiles of Fe-Pz2Py measured along the Fe2p and N1s binding regions, respectively. The bold lines represent the adsorption-deconvolution analysis using an admixture of Gaussian-Lorentzian functions.

The recorded XPS absorption envelopes of Fe-Pz_2Py in the Fe2p (Figure 2c) and N1s energy windows (Figure 2d) allow to further substantiate the spin and oxidation state of the iron centre in the neat complex before loading into GO. The Fe2p binding energy exhibits three dominant signals consistent with the presence of high-spin Fe(II). These signals are assigned a $Fe2_{p3/2}$ (713.3 eV), $Fe2_{p3/2}$ (718.5 eV, satellite), and $Fe2_{p1/2}$ (726.9 eV). In addition, a small satellite peak falling at higher energy (731.5 eV, $Fe2_{p1/2}$) is detected. The high spin nature (S = 2) and oxidation state of the ferrous cation has been ultimately confirmed by ^{57}Fe Mössbauer spectroscopy (at T = 300 K and at T = 5 K in an absence of an external magnetic field), showing one clean doublet in the entire temperature range. The ^{57}Fe Mössbauer spectra are given in Figure 4a for the envelope observed at 300 K (with an isomer shift, δ, of 0.95 mm/s and quadrupole splitting, Δ, of 2.48 mm/s) and in the Supporting Material (ESI, Figure S2) for the measurement performed at 5 K (δ = 1.06 mm/s and Δ = 3.31 mm/s).

Synthesis and physical properties of the hybrid system, Fe-Pz_2Py/GO. The self-assembly process of GO with Fe-Pz_2Py (Fe-Pz_2Py/GO, hybrid system) is obtained easily by mixing together diverse proportions of these two components (in weight) in DMF solution, followed by precipitation and purification of the hybrid material through consecutive centrifugation and washing steps (EtOH). In particular, prior to the attachment of Fe-Pz_2Py, GO was treated with NaOH in water (see sample preparations in Materials and Methods). The process allows formation of additional oxygen functional groups onto the GO basal plane and, at the same time, assists in the removal of even minute traces of metal-salts impurities during the washing steps. From the analysis of the *zeta*-potential (in water), Fe-Pz_2Py exhibits positive surface charges of +20.5 mV. On the contrary, pre-treaded GO shows negative surface charges, of -31.5 mV. The charge differences allow easing the loading process, by coupling together electrostatic and π-π interactions as driving forces for the material's assembly. The variation of the *zeta*-potential following the addition of Fe-Pz_2Py to GO is shown in Figure 3a. The negative charges of GO become gradually quenched in the hybrid system, and formation of the composite material (GO-drug) occurs smoothly. However, when the Fe-Pz_2Py and GO ratios becomes higher than 0.85, precipitation of the hybrid follows within minutes, in both DMF and water solutions (*zeta*-potential less than -5 mV in water). Therefore, we used low loading (16% in weight, zeta-potential = -20 mV) of Fe-Pz_2Py onto GO in a way to obtain material suitable for biological testing.[36-38] The low Fe-Pz_2Py/GO ratio granted formation of a hybrid system very stable in the water medium, showing no leakage of Fe-Pz_2Py over time (see in ESI, DTA/TG%/DTG analysis, Figure S5). The X-ray powder diffraction pattern of untreated GO compared to pre-treated GO (in NaOH) and Fe-Pz_2Py/GO, containing the 0.16 loading ratio, is shown in Figure 3b within the 2θ range of 2.5°–30°. The typical diffraction signatures of GO clearly emerge in the spectra, with strong reflection at scattering angles 2θ ~ 10°–11°. These peaks are associated to a $d_{0\,0\,1}$ spacing of 7.8 Å (untreated GO, lower line), 8.5 Å (pre-treated GO, middle line) and 8.3 Å (Fe-Pz_2Py-GO, upper line) as calculated from the Bragg's law. The post-synthetic treatment of GO with NaOH allows the creation of additional oxygen functional groups, which leads to an enlargement of the

interlayer space in response to the increased material's volume. Following the loading of Fe-Pz_2Py, the interlayer space slightly decreases. It is important to note that the observed effect does not fully validate the successful intercalation of Fe-Pz_2Py into the interlayer space of GO; however, given that a GO layer possesses a ~6.1 Å width, and upon counting its oxygen functional groups,[39] the effective space in the hybrid remains larger than 2.2 Å (*i.e.* 8.3-6.1 Å), and thus such void may accommodate a π-stacking arrangement of Fe-Pz_2Py onto the GO planes. In addition, comparing with NaOH treated GO, which have highly negative charge and thus strong repulsion action between GO sheets, loading of Fe-Pz_2Py results in screening the repulsion, and hence, the decrease of the *d*-space in Fe-Pz_2Py/GO is expected. Further evidences of the effective loading of Fe-Pz_2Py into GO and its orientation in respect to the GO surface are given by X-ray photoelectron spectroscopy (XPS) measurements. The C1*s* and Fe2p core level from the XPS measurements of the hybrid Fe-Pz_2Py/GO are shown in Figure 3c and Figure 3d, respectively. Following deconvolution with mixed Gaussian–Lorentzian functions, the C1s core spectrum (Figure 3c) is found to consist of six components. In particular, peaks at 284.6 eV (6.8%), ~285.6 eV (9.5%), ~286.8 eV (39.9%), 287.8 eV (10.4%), ~288.8 eV (29.2%), and ~290.2 eV (4.2%) are tentatively assigned to C-C/C-H bonds, C-O/C-N bonds, C-O-C epoxide/ether groups, C=O carbonyl groups, COO^- carboxyl groups, and π-π interactions in that order.[40-41] The Fe2*p* core level XPS spectrum of the hybrid material is shown in Figure 3d; since neat GO does not contain iron or nitrogen atoms these findings validate the formation of the Fe-Pz_2Py/GO hybrid (see also XPS spectrum of Fe-Pz_2Py in the N1s energy window, ESI, Figure S6). Furthermore, the slight shift of the main Fe2$p_{3/2}$ peak (at 713.9 eV) compared to the correspondent core transition observed in the isolated Fe-Pz_2Py complex (at 713.3 eV, Figure 2c) suggests that some modifications of the chemical environment and/or oxidation of the Fe(II) cations occur upon interaction with GO. While no significant shifts in the Raman spectrum of the hybrid materials is observed following the Fe-Pz_2Py intercalation, as evidenced from the unperturbed D-band (1345 cm^{-1}) and G-band (1598 cm^{-1}) of GO (Supporting Material, Figure S4), a shift of the carbonyl groups' band is observed in the FT-IR spectrum, from 1629 cm^{-1} in neat GO to 1645 cm^{-1} in the hybrid Fe-Pz_2Py/GO (ESI, Figure S3). The shift in this signal may indicate that the carboxylic acid groups located on the GO edges can act as additional ligands for the iron cation of the Fe-Pz_2Py complex. Thus, it is highly probable that similar behaviour may emerge for those anticancer drugs, e.g. Ruthenium-based and Pt-based, that usually contain exchangeable and/or weakly bound ligands.

The presence of such weak ligands for the metal cation provides the chemical basis for DNA binding and allows expressing their effective cytotoxicity in cancer therapies. The magnetic properties of the hybrid system recorded in the temperature range 2-300 K are shown in Figure 2b (lower trace). The result clearly confirms the formation of a spin-active material with magnetic trend consistent with the effective loading of Fe-Pz_2Py onto GO ((emu/g) × *T* at 300 K = 0.0027). However, the (emu/g) × *T* product is larger than that expected for a 16% loading of *S* = 2 system, and points towards an alteration of the iron oxidation-state and spin-state upon loading into GO. In order to shed more lights onto the oxidation and spin state of the iron in the GO-drug conjugate, ^{57}Fe Mössbauer spectroscopy was finally employed.

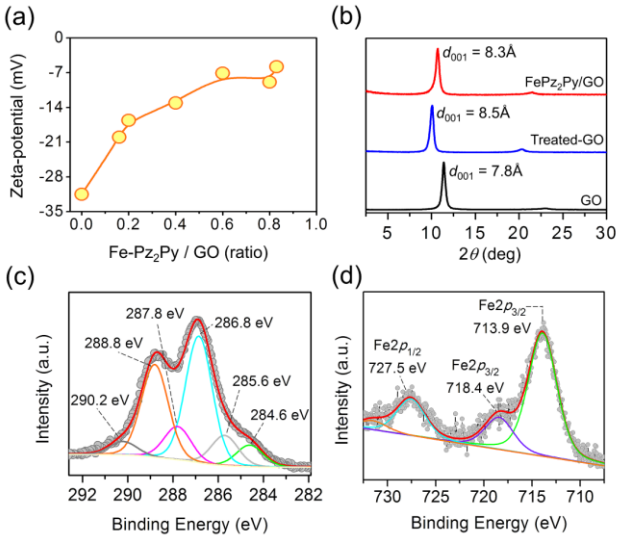

Figure 3. Panel **(a)** shows the zeta-potential variation (in water) of GO upon increasing the loading of Fe-Pz_2Py, expressed as ratio (weight/weight). Panel **(b)** illustrates the XRD profiles of GO (black line) compared to OH enriched GO (blue line) and the hybrid material (red line). Panel **(c)** and **(d)** show the XPS absorption profiles of hybrid material measured along the $C1_s$ and $Fe2_p$ binding regions, respectively. The adsorption-deconvolution analysis using an admixture of Gaussian-Lorentzian functions is shown by bold lines.

The room-temperature ^{57}Fe Mössbauer spectrum of the Fe-Pz2Py/GO hybrid shows only one doublet component (Figure 4b), similar to the case observed in the neat Fe-Pz_2Py complex. However, both isomer shift and quadrupole splitting parameters are shifted to lower values. More specifically, δ and Δ equals to 0.32 mm/s and 0.75 mm/s, respectively, and these values are typical signatures for Fe(III) in a high-spin state (*S* = 5/2). Thus, the interaction of GO with Fe-Pz_2Py complex alters the iron oxidation state, draining electrons from Fe-Pz_2Py to GO. The active electronic link between Fe-Pz_2Py and GO is further supported by the clear asymmetry of the ^{57}Fe Mössbauer doublet, suggesting that the averaged dominant configuration is a stacking orientation of the Fe-Pz_2Py complex with respect to the GO plane. In such scenario there is around the probed Fe nucleus in Fe-Pz_2Py a higher degree of anisotropy in the electric field gradient. It should be pointed out that only Mössbauer spectroscopy was able to provide clear evidences of the oxidation and spin state alteration of the drug upon loading; thus, it is highly challenging to discover similar effects in drugs based on redox susceptible metal complexes that do not contain iron cations.

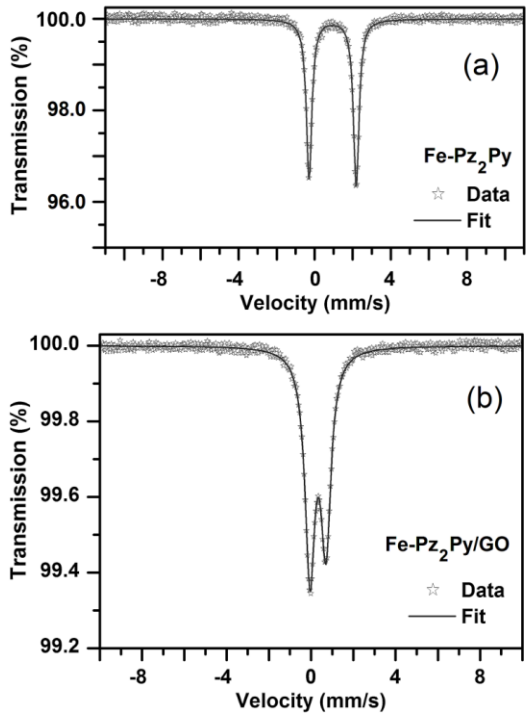

Figure 4. Room-temperature ^{57}Fe Mössbauer spectrum of the **(a)** Fe-Pz_2Py complex and **(b)** Fe-Pz_2Py/GO hybrid.

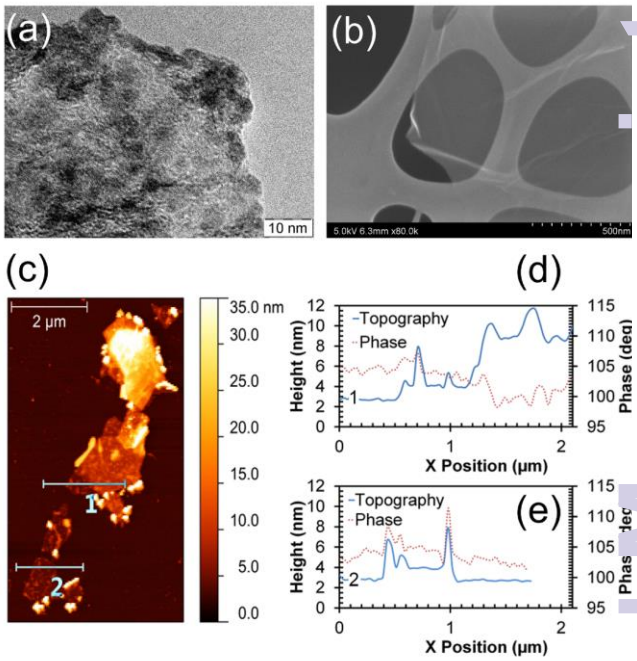

Figure 5. The Panel **(a)** shows the TEM and **(b)** the SEM micrographs of the water dispersion of the hybrid material Fe-Pz_2Py/GO deposited on a copper grid. Panel **(c)** shows the semi-contact atomic force microscopy scan of Fe-Pz_2Py/GO on muscovite mica. Panel **(d)** and panel **(e)** show the line profiles together with the phase-lag along the directions (1) and (2) shown in panel **(c)**.

Morphological organization of the hybrid system, Fe-Pz_2Py/GO. The morphological organization of Fe-Pz_2Py/GO emerges more clearly from analysis of the TEM (Figure 5a) and AFM (Figure 5c) micrographs. The SEM picture is provided in Figure 5b and in the Supporting Material (ESI, Figure S7, SEM and TEM additional micrographs). The micrometer-size sheets of GO are covered non-homogeneously by Fe-Pz_2Py (Figure 5a), especially along the GO edges and on the GO wrinkles, indicating that in these areas occur a large accumulation of Fe-Pz_2Py. This phenomenon is not surprising. Excess of negative charges and the carboxylic acid groups, capable to coordinate Fe-Pz_2Py, are thought to be located mainly in these areas, on the wrinkles and on the boundaries of the GO-sheets, respectively. The results obtained from the semi-contact atomic force microscopy (AFM) experiments on the hybrid material provide further support to this un-even localization of Fe-Pz_2Py onto GO (Figure 5c). The phase lag collected during the AFM measurement differs in fact between the multilayered GO and the single layer GO, property that implies different types of interactions with the scanning probe.[42] The AFM micrographs reveal, in addition, the presence of small surface features on the plane of the GO flakes; the smallest are estimated to encode dimension of 10.2±3.3 Å in length on the multilayer flakes and 12.9±1.6 Å on the single layer flakes (Figure 5d-e). The sizes of these components are therefore compatible with the dimension of a flat positioning of Fe-Pz_2Py (from DFT calculation, the complex encodes 10.8 Å lateral size) lying on the GO plane.

The cytotoxic impact of neat Fe-Pz_2Py, neat GO and Fe-Pz_2Py/GO. The proclivity of Fe-Pz_2Py and the hybrid system to alter cell's cycle and to potentially act as cytotoxic drug/vector-drug conjugate is, by design, very different; for Fe-Pz_2Py, the small molecule size and positive charges may favour its fast endocytosis, leading the organometallic complex through the nuclear pore channels; hence Fe-Pz_2Py should target preferentially the nuclear DNA, similar to DOX, Pt-based and Ruthenium-based drugs. For Fe-Pz_2Py/GO, the micro-meter size of the GO sheets and the excess of negative charges should prevent its fast incorporation into the cells by macropinocytosis, and thus the cytotoxic impact of neat GO as well as Fe-Pz_2Py/GO is exerted mainly at extracellular level, acting on the functionality and integrity of the cell's membrane. These different ways of action can be clearly seen in Figure 6b-6e, showing the optical micrographs of L929 mouse fibroblasts cell line incubated with increasing amounts of Fe-Pz_2Py (Figure 6b,6d), and Fe-Pz_2Py/GO (Figure 6c,6e). For example, from the inset in Figure 6e, the micro-meter size flakes of the GO-drug conjugate, Fe-Pz_2Py/GO, covers large part of the outer cell's membrane in a way that induces cell's apoptosis. Such cytotoxic effect arising from the interaction between cells and nano/micro-sized GO platelets is known in literature.[1,8,11] Adhesion of GO to the cell's membrane can alter the cell ultrastructure, morphology, and induces oxidative stress combined with complex alteration of the metabolic activity as described, for example, by Lammel T. and co-authors on Hep G2 cells (human hepatocellular carcinoma). Because Fe-Pz_2Py exhibits fluorescence emission in the range

300-450 nm at the excitation wavelength of 295 nm, this property allows studying directly the interaction of Fe-Pz_2Py with DNA and the individual base-pairs *via* fluorescence quenching experiments. We observed that the emission maximum and shape of the peaks caused a concentration dependent quenching of the intrinsic fluorescence of Fe-Pz_2Py being accompanied with hypochromism when DNA, thymine and cytosine are used as quenchers (ESI Figure S11). The fluorescence quenching phenomenon, on the other hand, is found negligible for adenosine and guanine. Fe-Pz_2Py is thus capable to exert, as anticipated earlier, two effects, (i) intercalation (DNA) and (ii) the specific recognition/binding of nucleotide bases (thymine and cytosine). Therefore, Fe-Pz_2Py represents a viable alternative for ruthenium and platinum based anticancer drugs, as well as antibiotic such as DOX. Different groups have demonstrated that depending on the structure and environment of the ruthenium complexes, the complexes interact with DNA by intercalation, cross-linking or ionic interactions to cause DNA damages in cancer cells.[44-47] In particular, Chao et al. has shown that an important structural property of the ruthenium complexes that enhances affinity in the DNA binding is associated to the ligand planarity of the complex.[48] This structural factor is encoded by chemical design in Fe-Pz_2Py. Analysis of the linear plot obtained in the quenching process according to Equation (1) allows estimation of the two constants *K* and *n,*

$$\log[(F_0-F_f)/F_f] = \log K + n \log[Q] \quad (1)$$

where the term $[(F_0-F_f)/F_f]$ represents the fluorescence quenching (F_0, initial; F_f, final), [Q] the concentration of the quencher, *K* the binding constants and *n* number of binding sites. The results give *K* of 7.9 ± 1.6 M^{-1} for DNA, 5.0 ± 1.1 M^{-1} for thymine and 0.04 ± 1 M^{-1} for cytosine with *n* being equal to 1.8 ± 0.2 for DNA, 1.2 ± 0.05 for thymine and 0.05 ± 0.005 for cytosine. These values clearly indicate that the interaction between Fe-Pz_2Py and DNA is the strongest, since it can couple both phenomena (intercalation and binding), followed by site recognition and binding only, for thymine and cytosine (ESI, Figure S9 and Figure S10-S11). Similar experiments for the hybrid material were not carried out, because of the severe fluorescence quenching of Fe-Pz_2Py upon interaction with GO combined with its inability, on average, to cross easily the cell's membrane. The biological impacts of Fe-Pz_2Py, GO and Fe-Pz_2Py/GO were analysed in terms of cell's cytotoxicity using combination of MTT and ROS assays. The MTT test allows unveiling the effects of these materials on the cell's growth in conjunction with the screening of the cell's mitochondrial activities (Figure 6f-6g). Addition of neat Fe-Pz_2Py, neat GO and Fe-Pz_2Py/GO to L929 mouse fibroblasts cell line shows in all cases a clear decrease of the cell's viability upon increasing their concentration. The IC_{50} (half-inhibitory concentration) accounts for 73 µg/mL for Fe-Pz_2Py, 64 µg/mL for neat GO and 82 µg/mL for the Fe-Pz_2Py/GO hybrid (approximately 13 µg/mL loaded $FePz_2Py$) (Figure 6f), showing that the neat GO is substantially more toxic than the hybrid system. Our observed value for neat GO is in harmony with the averaged IC_{50} known for such material.[8,49] It is often stated that the clear advantage of using GO as a drug-vector for biomedical applications is associated to the fact that hydrophobic drugs can be loaded in high amount into the hydrophilic GO-scaffold. Although true, the statement does stand only in the case when it is clearly demonstrated that the drug is not altered upon interaction with GO and *vice versa*. When such scenario occur, as shown in this work, the bottom-up improvement of the GO-composites designed for drug's transport become more complex to devise. In order to shine lights into the mechanism of cell's apoptosis and on the specific cytotoxic impact of these materials, the reactive oxygen species generation (ROS) was studied in the presence of Fe-Pz_2Py, Fe-Pz_2Py/GO and neat GO. The addition of Fe-Pz_2Py into L929 cell lines shows no significant ROS formation in a wide range of concentration (Figure 6g). The data are therefore consistent with its envisioned mechanism of action, in which endocytosis of Fe-Pz_2Py leads to intercalation/binding of the DNA base pairs. On the contrary, the ROS screening using the hybrid material and neat GO shows generation of reactive oxygen species. While neat GO is capable to produce significant ROS already at concentration as low as 40 µg/mL (Figure 6g), the presence of Fe-Pz_2Py in the hybrid, following its alteration in the metal oxidation state, decreases the formation of reactive oxygen species. Thus Fe-Pz_2Py acts as an electron-buffering agent, down-regulating the generation of ROS by nearly one third of the value witnessed for neat GO. Such ability of GO to generate reactive oxygen species is thought to be linked with the complex interplay of structural factors (size), composition (C/O ratios), aggregation proclivity as well as with the presence of trapped impurities.[8,11,50] GO contains sp^2 and sp^3 carbon centres, together with epoxy and tertiary hydroxyl groups on the basal plane. Keto, carboxylic acid and ester groups are also present in various percentages in the GO sheets, according to the specific degree of the material's oxidation. These groups are mainly placed at the edges of the sheets, but carbonyl moieties can also be formed at the edges of holes present in the GO plane.[51] These carbon-oxygen containing sites are the reactive centres, from the chemical, red-ox and toxicological perspectives, but also topological defects, the presence of structural vacancies, adatoms, and edges/cracks in the GO layer[52-54] may contribute as well to enhance the GO toxicity and reactivity upon its exposure to biological molecules, such as membrane lipids and cellular red-ox complements present in the cytoplasmic matrix.[55-58] The red-ox proclivity of GO towards other red-ox active systems, as witnessed here for Fe-Pz_2Py within the assembly process of the hybrid material (Fe-Pz_2Py/GO), find some parallelism with the recent work of Liu S. and co-workers, in which oxidation of the glutathione molecule (as probed in *Escherichia coli*) is promoted by GO sheets, process that allows to additionally envision the use of GO as antimicrobial agent.[59] However, when GO is envisioned as carrier in drug delivery, such reactivity and cytotoxicity of GO is certainly not a desirable property to bring in the final drug-GO conjugate material. Therefore, down-regulating its intrinsic reactivity and toxic impact is vital.

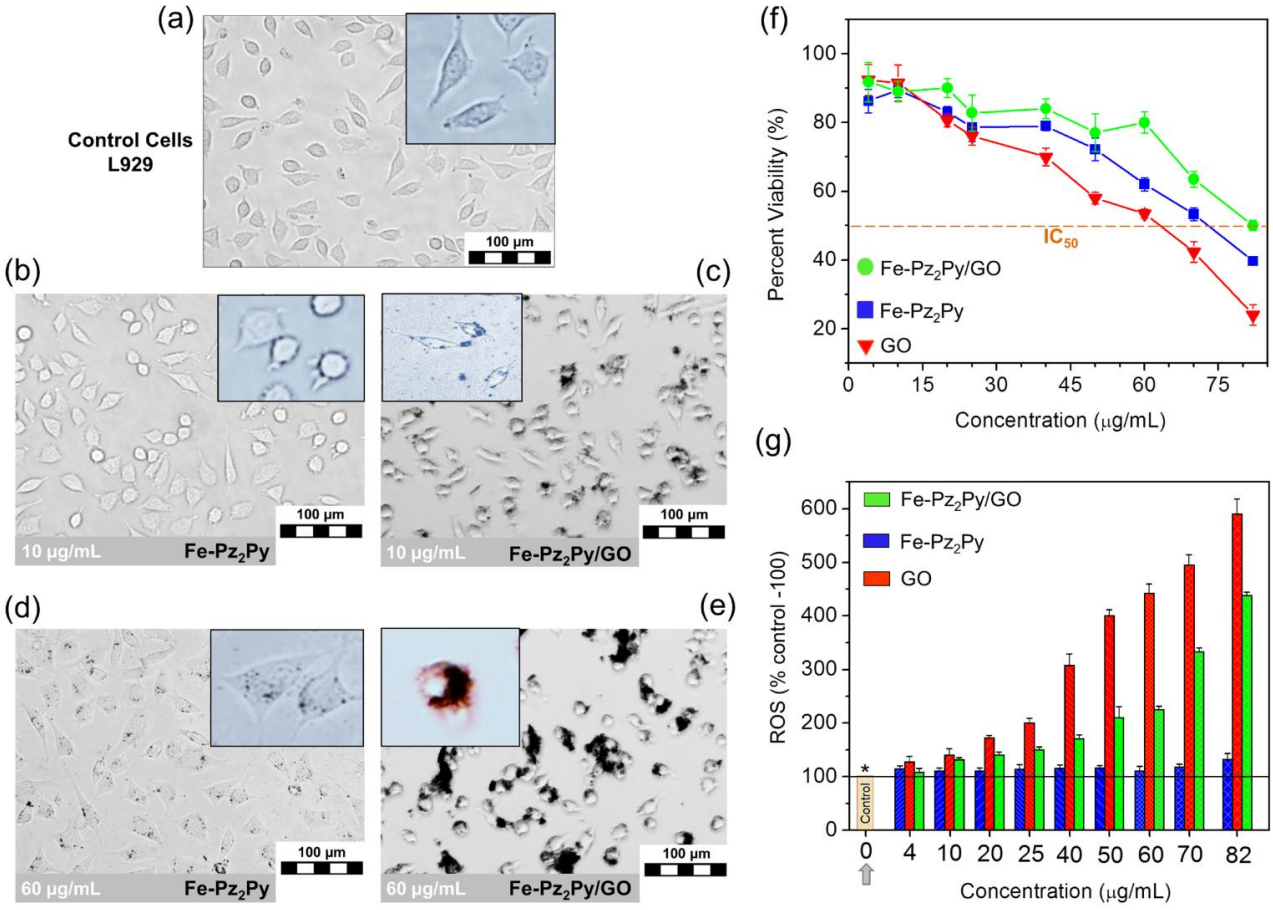

Figure 6. The confocal microscopy images of the mouse fibroblast L 929 cells culture without **(a)** and with **(b-e)** increasing amounts of Fe-Pz_2Py (10 µg/mL in panel b, 60 µg/mL in panel d) or Fe-Pz_2Py/GO (10 µg/mL in panel c, 60 µg/mL in panel e). Cells were maintained at 37°C with 5% humidified CO_2 in an incubation chamber for 24 hours. Images were collected using an optical microscope (Olympus IX 70) with an objective of 40×. Panel **(f)** shows the impact on the cell's viability (L 929 mouse fibroblasts) versus increasing concentration of neat Fe-Pz_2Py (squares), neat GO (triangles) and Fe-Pz_2Py/GO (circles). Panel **(g)** shows the ROS formation (% - 100(control)) in L 929 mouse fibroblasts cell line in presence of Fe-Pz_2Py, GO and Fe-Pz_2Py/GO. The thin-line (black) in **(g)** and the yellow-bar are guides to the eyes and show the reference base-line (100, no detectable ROS, control cells only).

As mentioned earlier, among the diverse synthetic strategies used to enhance the biocompatibility of GO, the GO-sheets functionalization has been widely pursued. Different polymers have been used to create GO-functionalized materials and tested *in vitro*, such as GO decorated with polyethylene glycol (PEG), polyacrylic acid (PAA), polyethylenimine (PEI), amphiphilic copolymers, poly(vinyl) alcohol, and sugars (e.g. chitosan, alginate).[1,8,9,11] In particular, numerous studies demonstrated that GO functionalized with PEG chains exhibits negligible *in vitro* toxicity against a variety of cell lines, including MCF-7, MDA-MB-435, Raji, HCT-116, OVCAR-3, U87MG, as well as decreased toxicity is observed for *in vivo* models, such as nematodes (*Caenorhabditis elegans*).[8e,9a,11,60] On the contrary, the *in vivo* toxicity of neat GO observed in *Caenorhabditis elegans*, shows that prolonged exposure to 0.5–100 mg L^{-1} of GO causes severe damages on functions of both primary (intestine), secondary targeted organs (neuron and reproductive organ) and severe accumulation of pathogenic microbial food in the intestine.[60,61] Other approaches used to mitigate the cytotoxicity of GO have also been explored, and, among others, the use of higher concentration of fetal bovine serum (FBS, 10%), a widely used serum-supplement added to cells culture, appears very promising.[62] Here, the decreased toxicity of GO nano-sheets, which produce also physical damages to the cell's membrane, is largely reduced by the strong adsorption proclivity of FBS onto the GO basal plane. Therefore, a combination of those aforementioned strategies (surface functionalization of GO) may generate improved GO vectors for biomedical use; our finding clearly warns on the use of metal based drugs loaded into neat GO without post synthetic control of the red-ox integrity of the GO-drug conjugate, but it also offers a novel ground of exploration for

biocompatible GO systems in drug-delivery. Together with polymers (e.g. PEG) and/or FBS/protein decorated GO-sheets, red-ox active components, likewise Fe-Pz_2Py, could be further considered in the assembly of multi-components GO vectors, so to add red-ox regulators for boosting further their minimal cytotoxic impacts.

Conclusions

The self-assembly process of a mononuclear iron (II) complex with graphene oxide (GO) micrometer-sheets, as obtained through combination of π-π and electrostatic interactions in solution, clearly revealed the reactive nature of the neat graphene oxide carrier, and invokes a careful reconsideration of its role as drug delivery system for biomedical applications, especially for the loading of metal-based drugs. The neat iron complex was found highly effective in disrupting cell's cycle through DNA binding, sharing cytotoxicity behaviour and potency similar to doxorubicin and ruthenium-based anticancer compounds. However, in the hybrid material, electron transfer occurred from the iron (II) complex to the GO support and the emergence of this process down-regulated the proclivity of GO to produce reactive oxygen species *in vitro*. Such alteration in the chemical/physical integrity of the anticancer metal-drug loaded into GO, unless unveiled and controlled, can ultimately prevent the clear bottom-up engineering of theranostic GO delivery platforms, and our findings provide a case-study that highlights such non-innocent nature of GO based-materials as drug delivery systems.

Experimental Section

Chemicals: All reagents were purchased of the highest grade commercially available and were used as received (potassium metal, 2,6–dibromopyridine, pyrazole, diglyme, THF, graphite and $FeCl_2 \times 4H_2O$).

Synthesis of the Pz_2Py and Fe-Pz_2Py. The 2,6-bis(pyrazol-1-yl)pyridine (Pz_2Py) was synthesized following published procedures[31] but purified differently.[32] The mononuclear iron complex, Fe-Pz_2Py, was synthesized and purified according to the literature procedure.[33] Elemental analysis for Fe-Pz_2Py; found: C, 33.50; H, 3.92; N, 17.74, calculated for $C_{11}H_9Cl_2FeN_5 \times 3H_2O$: C, 33.70; H, 3.86; N, 17.86. FT-IR, DTA/TG%/DTG and UV-Vis spectra are given in ESI, Fig. S3, S5 and S8, respectively.

Synthesis of GO and GO enriched with OH groups. Graphene oxide (GO) was synthesized using a modified Staudenmaier method.[63,64] 1 g graphite (Fluka, 50870) was dispersed in 20 mL HNO_3 65 wt% and 40 mL H_2SO_4 96 wt% in a 100 mL spherical flask. Solution was stirred for 30 min at ~0 °C with an ice-bath. 20 g $KClO_3$ 98% were gradually added and stirring was continued for 20 h at room temperature (RT). The solution was then added to 200 mL H_2O and GO was obtained by six centrifugation steps (2700 rcf, 5 min) with interval rinsing with H_2O until the pH value of the supernatant solution reached pH = 6. GO was air-dried at RT. Prior to the attachment of Fe-Pz_2Py, GO was further treated with NaOH for the creation of additional oxygen functional groups (GO-enriched in C'' groups). For the functionalization, 200 mg GO were initially dispersed in 50 mL H_2O with sonication in water bath for 1 h. 50 mL of a NaOH 3M solution were added and sonication was continued for additional 3 h. HCl 37 wt% was added to nearly neutralize the solution and GO was obtained by centrifugations (2700 rcf, 5 min) with interval rinsing with H_2O until the pH value of the supernatant solution went below pH = 8. The GO-enriched sample was air-dried at RT and used for the synthesis of the hybrid material Fe-Pz_2Py/GO.

Synthesis of the hybrid material Fe-Pz_2Py/GO. 60 mg of GO were dispersed in 25 mL DMF with sonication in water-bath for 30 min. Then, the suspension was added in a flask containing 30 mg of Fe-Pz_2Py under nitrogen atmosphere and the so-formed mixture was stirred for 24 h. Fe-Pz_2Py/GO was obtained by centrifugations (2700 rcf, 5 min) with interval rinsing with EtOH and air-dried at RT. The final effective loading of Fe-Pz_2Py onto GO was found to be 16% in weight, as estimated from atomic absorption experiments on the total iron content and TGA/DTA analysis. This loaded amount of Fe-Pz_2Py appeared tightly loaded into the GO layers and was not washed out either from prolonged water washing or the prolonged storage of Fe-Pz_2Py/GO in water (weeks).

Analytical measurements and Theory

X-ray powder diffraction data (**XRD**) were collected with a D8 Advance Bruker diffractometer using Cu$K\alpha$ (40 kV, 40 mA, λ=1.54178 Å) radiation. Diffraction patterns were collected in the 2ϑ range from 2 to 80°, in steps of 0.02° and 2 s counting time per step.

X-ray photoelectron spectroscopy (**XPS**) measurements were performed under ultrahigh vacuum conditions with a base pressure of 5×10^{-10} mbar in a SPECS GmbH instrument equipped with a monochromatic Mg$K\alpha$ source (hv = 1253.6 eV) and a Phoibos-100 hemispherical analyzer. Pulverized samples were dispersed in H_2O (1 wt%), and after short sonication and stirring, a minute quantity of the suspensions was drop cast on silicon wafers and left to dry in air before transfer to ultrahigh vacuum. The energy resolution was set to 0.3 eV and the photoelectron take-off angle was 45° with respect to the surface normal. Recorded spectra were the average of 3 scans with energy step set to 0.05 eV and dwell time 1 sec. All binding energies were referenced to the C1*s* core level at 284.6 eV. Spectral analysis included a Shirley background subtraction and peak deconvolution employing mixed Gaussian–Lorentzian functions, in a least squares curve-fitting program (WinSpec) developed at the Laboratoire Interdisciplinaire de Spectroscopie Electronique, University of Namur, Belgium.

Thermo-gravimetric analysis (**TG**) and differential thermal analysis (**DTA**) were performed using a Perkin Elmer Pyris Diamond TG/DTA instrument. Samples of approximately 3-3.5 mg were heated in still air from 25 °C to 800 °C, with a 5 °C/min heating rate (Supporting Material, Figure S5).

Transmission electron microscope (TEM) micrographs were taken on a JEOL 2010 microscope operating at 160 kV with a point-to-point resolution of 1.9 Å. Before measurements, the aqueous suspension of Fe-Pz_2Py/GO (1 mg /mL) was diluted with DI water (5 mL), and treated in ultrasound water-bath for 5 minutes. A drop of the dilute suspension was placed onto a holey-carbon film supported by a copper-mesh TEM grid and air-dried at room temperature.

Scanning electron microscope (SEM) micrographs were taken on a Hitachi 6600 FEG microscope. The sample preparation was obtained as reported above in the TEM measurements.

Atomic absorption (AO). The total content of iron present in the samples (Fe-Pz_2Py and Fe-Pz_2Py/GO) was determined by atomic absorption spectroscopy (AAS) with flame ionization using Perkin Elmer 3300 device (Perkin Elmer, USA) at 248.3 nm. The samples were pre-digested in concentrated HNO_3 acid (70%) and then diluted with DI water to obtain 2% HNO_3 (w/vol) solutions.

Fourier transform infrared (FT-IR). Pellets of pulverized samples dispersed in KBr were used for recording the spectra using a Perkin Elmer GX Fourier transform spectrometer in the frequency range of 400–4000 cm^{-1}. The reported spectra are an average of 64 scans with 2 cm^{-1} resolution (Supporting Material, Figure S3).

Raman spectroscopy. Raman spectra were recorded with a micro-Raman (μ-Raman) Renishaw RM1000 system using a laser diode excitation line at 532 nm in the frequency range of 200–3500 cm^{-1}. Raman scatter was collected by means of an Olympus optical microscope, equipped with 50× and 100× lenses. Using the 100× lens, the probing spot was about 1 μm in diameter. The laser power was set to 5 mW. The spectrometer was calibrated by recording the spectrum from a Si sample with characteristic Raman peak at 520.7 cm^{-1}. Raman spectra were obtained either from samples in the form of small flakes or from thin films for which minute quantities of samples' aqueous suspensions were drop casted onto a glass substrate and left to dry in air before measurements. The reported spectra are an average of 5 scans (Supporting Material, Figure S4).

Zeta-potentials of Fe-Pz_2Py, GO and Fe-Pz_2Py/GO were measured in water solution on a Zetasizer Nano particle analyser ZEN3600 (Malvern Instruments, UK) at T = 298 K.

Bulk magnetic susceptibility were measured using a superconducting quantum interference device (SQUID, MPMS XL-7, Quantum Design, USA) in the temperature range of 2 K - 300 K under an external magnetic fields of 1000 kOe.

Atomic Force microscopy (AFM). Following sonication (3 min, water bath, room temperature) of a diluted solution of Fe-Pz_2Py/GO (water, 1 mg /10 mL) the suspension was deposited onto a fresh cleaved muscovite green mica surface and dryed in an exicator under low pressure at room temperature. The topography and phase image of Fe-Pz_2Py/GO was obtained on a NTegra Prima with a HA-NC probe (Moscow) in the semicontact mode. The scanning speed for the phase image was set to 6033 nm/s while the set point for the amplitude was 7.01nA compared to the 13nA of the free amplitude.

^{57}Fe Mössbauer spectroscopy. The transmission ^{57}Fe Mössbauer spectra were measured using a Mössbauer spectrometer operating in a constant acceleration mode and equipped with a 50 mCi ^{57}Co(Rh) source. The samples were placed inside the chamber of a closed-helium cycle device providing setting of temperatures in the range from 5 to 300 K. The recorded ^{57}Fe Mössbauer spectra were fitted using the MossWinn software package; the isomer shift values are referred to metallic α-Fe at room temperature.

Theoretical calculations. The theoretical modelling and geometry optimization of the Fe-Pz_2Py complex coordinated by three water molecules, mimicking its hydrated form, was carried out by density functional theory (DFT) in gas phase using unrestricted M06 function (Exchange: 0.2700 Hartree-Fock + 1.0000 M06)[65] with the EML grid (70, 302) and basis set 6-31G* for the C/H/N/O atoms and LanL2DZ basis for the Fe atom, as implemented in the computational package Sparta. 14.[66] The SCF convergence was set to 10^{-7} au for the energy change and for the gradient convergence was set below 0.0003. The optimized structure converged to the point group c_2 and was validated by frequency calculation. The UV-Vis envelope of Fe-Pz_2Py was calculated by single point on the optimized structure by TDDFT-UEDF2/6-31G** (CIS = 30) employing frozen-core approximation. The calculated UV-Vis spectrum and input file is given in the Supporting Material (ESI, Figure S8).

Biological screenings

Cells Culture. L929 mouse fibroblasts cell lines and NIH 3T3 were cultured in a humidified, 37°C atmosphere comprised of 5% CO_2 and 95% room air. Cell culture medium, Dulbecco's Modified Eagle's medium (DMEM, Gibco) was supplemented with 10% fetal bovin serum (FBS, Sigma) and 5% penicillin/ streptomycin (Gibco). For MTT and Reactive Oxygen Species (ROS) assays, cells were plated 24 hours before experiments in a 96-well microtiter plates (TPP).

Cytotoxicity Assay Protocol. The cytotoxicity effects of Fe-Pz_2Py and Fe-Pz_2Py/GO on L929 cell lines were tested using a standard MTT assay (NIH 3T3 were used only for Fe-Pz_2Py). L929 (4×10^3) cell lines were incubated into 96-well microtiter plates with increasing concentration of Fe-Pz_2Py and Fe-Pz_2Py/GO water solutions (final concentrations of 5 – 100 µg/mL). After an incubation period of 24h, 10µL of MTT solution was added to each well and the plate was incubated once more for 1 hour at 37°C in 5% CO_2 and 95% air. This procedure allows the formation of formazan crystals for MTT analysis. The MTT / medium solution was removed and 100µL of DMSO were added. The plates were once again incubated on a shaker at room temperature for 15 min to solubilize completely the formazan crystals. Finally, the plates were recorded on a reader (Tecan, infinite M200 Pro) at 570 nm. Data were reported as means ± standard deviation (SD). The preparation of the MTT solution was as follow: the tetrazolium dye MTT was dissolved in phosphate buffered saline (PBS) to the concentration of 5 mg/mL. The solution was filtered and

sterilized through a 0.2 µM filter. The MTT solution was then stored and protected from light, at -20°C.

ROS Assay Protocol. The cytotoxicity effects of Fe-Pz_2Py and Fe-Pz_2Py/GO on L929 cell lines were tested using a standard ROS assay. L929 (4 x 10^3) cell lines was incubated into 96-well microtiter plates (TPP). The plates were incubated for 24 hours at 37°C in 5% CO_2. Different concentrations of Fe-Pz_2Py and Fe-Pz_2Py/GO water solutions (final concentration of 5 – 100 µg/mL) were added in triplicate. After an incubation period of 24 hours, the medium solution was removed, and the cells were washed 2 times with Hank's Balanced Salt Solution (HBSS). Then, 100 µL of DCFH-DA solution was added to each well. DCFH-DA solution (1µM) was prepared freshly by dissolving a stock solution of DCFH-DA (10mM) in HBSS. The plate was then incubated one more time for 1 hour at 37°C in 5% CO_2. Finally, the plate was recorded on a spectrofluorimeter (Tecan, infinite M200 Pro) at 495/530 nm.

UV-Vis. Salmon sperm DNA (DNA), Adenine (A), Guanine (G), Cytosine (C) and Thymine (T) were purchased from Sigma Aldrich and used without further purification. For the UV-Vis experiments, DNA, Adenine, Guanine, Cytosine and Thymine samples were dissolved in 50mM Tris pH = 8, while Fe-Pz_2Py was dissolved in water to form a stock solution of 0.3 mM. The UV-Vis samples were then prepared by addition of Fe-Pz_2Py and different concentrations of DNA or base pairs samples from the stock solution into water to give a final optical density at the excitation wavelength (290 nm) of 0.15. Fixing the concentration of Fe-Pz_2Py, different concentrations of DNA, and base pairs were made by adjusting the water. The molar extinction coefficient for salmon sperm DNA is 6 600M^{-1} cm^{-1} at 260nm.[67] Finally, the optical spectra of the various species were obtained using the SPECORD S 600 diode array (Analytik Jena, Germany).

Fluorescence. The same samples prepared for recording optical spectra (UV-Vis) were used to study their fluorescence. Fluorescence titrations were performed by adding into the cuvette the Fe-Pz_2Py solution and increasing amounts of DNA, Adenine, Guanine, Cytosine or Thymine. Steady-state fluorescence spectra and intensities in the quenching experiments were measured using a QuantaMaster 40 spectrofluorimeter (Photon Technology International, USA). The measurements were performed in 1.0 cm path-length cuvette at 25 °C. In the quenching experiments Fe-Pz_2Py, DNA, and base pairs concentrations were equal to 0.3mM. The data were recorded in the program FelixGX 4.1.2. (PTIGraphicX, U.S.A.). The mathematical treatments of the binding constants in the fluorescence quenching experiments are given in the Supporting Material, Figure S12.

Acknowledgements

Authors from Czech Republic thank the support of the Palacky University (institutional support), the Operational Program Research and Development for Innovations - European Regional Development Fund (project CZ.1.05/2.1.00/03.0058) and by the Operational Program Education for Competitiveness - European Social Fund (project CZ.1.07/2.3.00/20.0155 and 30.0004) of the Ministry of Education, Youth and Sports of the Czech Republic (LO1305) and the Grant Agency of the Academy of Sciences of the Czech Republic (KAN115600801; KAN200380801) and the Internal IGA grant of the Palacky University in Olomouc (IGA_PrF_2015_017). K. Dimos acknowledges the co-financed research by the European Union (European Social Fund – ESF) and Greek national funds through the Operational Program "Education and Lifelong Learning" of the National Strategic Reference Framework (NSRF) - Research Funding Program: THALES (377285).

Notes and references

1 M. Nurunnabi, K. Parvez, M. Nafiujjaman, V. Revuri, H. A. Khan, X. Feng,Y.-k. Lee, *RSC Advances,* **2015**, *5*, 42141-42161

2 (a) X. Yang, X. Zhang, Z. Liu, Y. Ma, Y. Huang, Y. Chen, *J. Phys. Chem. C*, **2008**, *112*,17554–17558. (b) Y.-M. Zhang, Y. Cao, Y. Yang, J.-T. Chen, Y. Liu, *Chem. Commun.*, **2014**, *50*, 13066-13069.

3 (a) L. Feng, S. Zhang, Z. Liu, *Nanoscale* **2011**, *3*, 1252–1257. (b) B. Chen, M. Liu, L. Zhang, J. Huang, J. Yao, Z. Zhang, *J. Mater. Chem.*, **2011**, *21*, 7736–7741.

4 C. He, Z.-Q.Shi, L. Ma, C. Cheng, C.-X. Nie, M. Zhou, C.-S. Zhao, *J. Mater. Chem. B*, **2015**, *3*, 592-602.

5 (a) L. Zhang, Y. Xing, N. He, Y. Zhang, Z. Lu, J. Zhang, Z. Zhang, *J. Nanosci. Nanotechnol.*, **2012**, 12, 2924–2928. (b) K. K. R. Datta, O. Kozak, V. Ranc, M. Havrdova, A. B. Bourlinos, K. Safarova, K. Hola, K. Tomankova, G. Zoppellaro, M. Otyepka, R. Zboril, *Chem. Commun.,* **2014**, *50*, 10782-10785.

6 (a) H. Zhu, L. Gao, X. Jiang, R. Liu, Y. Wei, Y. Wang, Y. Zhao, Z. Chai, X. Gao, *Chem. Commun.,* **2014**, *50*, 3695-3698. (b) Y. Liu, D. Yu, C. Zeng, Z. Miao, L. Dai, *Langmuir,* **2010**, *26*, 6158–6160.

7 S. R. Shin, B. Aghaei-Ghareh-Bolagh, X. Gao, M. Nikkhah, S. M. Jung, A. Dolatshahi-Pirouz, S. B. Kim, S. M. Kim, M. B. Dokmeci, X. S. Tang, A. Khademhosseini, *Adv. Funct. Mater.,* **2014**, *24*, 6136-6144.

8 (a) Y. Liu, Y. Luo, J. Wu, Y. Wang, X. Yang, R. Yang, B. Wang, J. Yang, N. Zhang, *Sci. Rep.*, DOI: 10.1038/srep03469. (b) L. -H. Liao, Y. –S. Lin, C. W. Macosko, C. L. Haynes, *ACS Appl. Mater Interfaces,* **2011**, *3*, 2607–2615. (c) Y. Chang, S. –T. Yang, J. –H. Liu, E. Dong, Y. Wang, A. Cao, Y. Liu, H. Wang, *Toxicol. Lett.,* **2010**, *200*, 201–210. (d) Y. Chang, S.-T. Yang, J.-H. Liu, E. Dong, Y. Wang, A. Cao, Y. Liu, H. Wang, *Toxicol. Lett.,* **2011**, *200*, 201-210. (e) A. B. Seabra, A. J. Paula, R. de Lima, O. Alves, N. Duran, *Chem. Res. Toxicol.,* **2014,** *27*, 159-168.

9 (a) Z. Liu, J. T. Robinson, X. M. Sun, H. Dai, *J. Am. Chem. Soc.,* **2008**, 130, 10876−10877. (b) Z. Xu, S. Wang, Y. Li, M. Wang, P. Shi, X. Huang, *ACS Appl. Mater. Interfaces,* **2014**, *6*, 17268-17276. (c) X. Zhao, L. Liu, X. Li, J. Zeng, X. Jia, P. Liu, *Langmuir,* **2014**, *30*, 10419-10429.

10 (a) O. Akhavan, E. Ghaderi, *ACS Nano* **2010**, *4*, 5731–5736. (b) H. Yue, W. Wei, Z. Yue, B. Wang, N. Luo, Y. Gao, D. Ma, G. Ma, Z. Su*, Biomaterials,* **2012**, *33*, 4013–4021. (c) W. Zhang, L. Yan, M. Li, R. Zhao, X. Yang, T. Ji, Z. Gu, J.-J. Yin, X. Gao, G. N. *Toxicology Lett.,* **2015**, *237*, 61-71. (d) F. Perreault, A. F. de Faria, S. Nejati, M. Elimelech, *ACS Nano* **2015**, **DOI:** 10.1021/acsnano.5b02067.

11 (a) X. Sun, Z. Liu, K. Welsher, J. T. Robinson, A. Goodwin, S. Zaric, H. Dai, *Nano Res.,* **2008**, *1*, 203-212. (b) J. Liu, L. Cui, D. Losic, *Acta Biomater.,* **2013**, *9*, 9243-9257.

12 B. Baguley and D. Kerr Eds. in *Anticancer Drug Development*, 2001, Academic Press, ISBN: 978-0-12-072651-6.

13 A. Wang, Z. Guo, *Chem. Soc. Rev*. **2013**, *42*, 202-224.

14 D. Wang, S. J. Lippard, *Nat. Rev. Drug Disc.* **2005**, *4*, 307-320.
15 S. H. van Rijt, P.J. Sadler, *Drug Discov. Today,* **2009**, *14*, 1089-1097.
16 C. G. Hartinger, S. Zorbas-Seifried, M.A. Jakupec, B. Kynast, H. Zorbas, B. K. Keppler, *J. Inorg. Biochem.,* **2006**, *100*, 891-904.
17 R. Trondl, P. Heffeter, C. R. Kowol, M. A. Jakupec, W. Berger, B. K. Keppler, *Chem. Sci.,* **2014**, *5*, 2925-2932.
18 Z. Adhireksan, G. E. Davey, P. Campomanes, M. Groessl, C. M. Clavel, H. Yu, A. A. Nazarov, C. H. F. Yeo, W. H. Ang, P. Dröge, U. Rothlisberger, P. J. Dyson, C. A. Davey, *Nat. Commun.,* **2014**, *5*, 3462.
19 (a) F. Arcamone, G. Cassinelli, G. Fantini, A. Grein, P. Orezzi, C. Pol, C. Spalla, *Biotechnol. Bioeng.,* **1969**, *11*, 1101–1110. (b) D. A. Gewirtz, *Biochem Pharmacol.,* **1999**, *57*, 727–741. (c) Y. –Q. Liu, W.-Q. Li, S. L. Morris-Natschke, K. Qian, L. Yang, G.-X. Zhu, X.-B. Wu, A.-L. Chen, S.-Y. Zhang, X. Nan, K.-H. Lee, *Med. Res. Rev.,* **2015**, *35*, 753-789.
20 L. J. Kershaw Cook, R. Mohammed, G. Sherborne, T. D. Roberts, S. Alvarez, M. A. Halcrow, *Coord. Chem. Rev.,* **2015**, *289-290*, 2-12.
21 M. A. Halcrow, *New J. Chem.,* **2014**, *38*, 1868-1882.
22 M. A. Halcrow, *Coord. Chem. Rev.,* **2005**, *249*, 2880-2908.
23 R. González-Prieto, B. Fleury, F. Schramm, G. Zoppellaro, R. Chandrasekar, O. Fuhr, S. Lebedkin, M. Kappes, M. Ruben, *Dalton Trans.,* **2011**, *40*, 7564-7570.
24 S. Vela, J. J. Novoa, J. Ribas-Arino, *Phys. Chem. Chem. Phys.,* **2014**, *16*, 27012-27024.
25 (a) G. Zoppellaro, A. Geies, V. Enkelmann, M. Baumgarten, *Eur. J. Org. Chem.,* **2004**, *11,* 2367-2374. (b) G. Zoppellaro, A. Geies, K. Kristoffer Andersson, V. Enkelmann, M. Baumgarten, *Eur. J. Org. Chem.,* **2008**, *8*, 1431–1440
26 T. D. Roberts, M. A. Little, F. Tuna, C. A. Kilner, M. A. Halcrow, *Dalton Trans.,* **2015**, *44*, 9417-9425.
27 M. Srinivasarao, C. V. Galliford, P. S. Low, *Nat. Rev. Drug Disc.,* **2015**, *14*, 203-219.
28 I. Ott, R. Gust, *Archiv der Pharm.,* **2007**, *340*, 117-126.
29 K. H. Thompson, C. Orvig, *Dalton Trans*., **2006**, 761-764.
30 R. Chakrabarty, P. S. Mukherjee, P. J. Stang, *Chem. Rev.,* **2011**, *111*, 6810-6918.
31 D. L. Jameson, K. A. Goldsby, *J. Org. Chem.,* **1990**, *55*, 4992–4994.
32 (a) G. Zoppellaro, M. Baumgarten, *Eur. J. Org. Chem.,* **2005**, *19*, 2888–2892. (b) G. Zoppellaro, M. Baumgarten, *Eur. J. Org. Chem.,* **2005**, *19*, 4201.
33 D. Gong, X. Jia, B. Wang, X. Zhang, L. Jiang *J. Organomet. Chem.,* **2012**, *702*, 10-18.
34 S. M. Zeman, D.R. Phillips and D.M. Crothers, *Proc. Natl. Acad. Sci. USA,* **1998**, *95*, 11561-11565.
35 N.-T. Chen, C.-Y. Wu, C.-Y. Chung, Y. Hwu, S.-H. Cheng, C.-Y. Mou and L.-W. Lo, *PLoS ONE,* **2012**, *7*, e44947.
36 R. Kurapati, J. Russier, M. A. Squillaci, E. Treossi, C. Ménard-Moyon, A. E. Del Rio-Castillo, E. Vazquez, P. Samorì, V. Palermo, A. Bianco, *Small,* **2015**, *11*, 3985-3994.
37 V. Georgakilas, M. Otyepka, A. B Bourlinos, V. Chandra, N. Kim, K C. Kemp, P. Hobza, R. Zboril, K. S Kim, *Chem. Rev.,* **2012**, *112*, 6156–6214.
38 C. Chung, Y. K. Kim, D. Shin, S. R. Ryoo, B. H. Hong, D. H. Min, *Acc. Chem. Res.,* **2013**, *46*, 2211-2224.
39 I. Dékány, R. Krüger-Grasser, A. Weiss, *Colloid Polym. Sci.* **1998**, *276*, 570-576.
40 V. Georgakilas, A. Demeslis, E. Ntararas, A. Kouloumpis, K. Dimos, D. Gournis, M. Kocman, M. Otyepka, R. Zboril, *Adv. Funct. Mat.,* **2015***, 25*, 1481-1487.
41 R. Y. N. Gengler, D. S. Badali, D. Zhang, K. Dimos, K. Spyrou, D. Gournis, R. J. D. Miller, *Nat. Commun.,* **2013**, *4*, 2560(1-5).
42 S. Zhang, H. Aslan, F. Besenbacher, M. Dong, *Chem. Soc. Rev.* **2014**, *43*, 7412-7429.
43 T. Lammel, P. Boisseaux, M.-L. Fernández-Cruz, J. M. Navas, *Particle and Fibre Toxicology*, **2013**, 10:27. doi:10.1186/1743-8977-10-27.
44 H. Mei and J. Barton, *J. Proc. Natl. Acad. Sci.USA,* **1988**, *85*, 1339-1343.
45 S. Smith, L. Finzi and C. Bustamante, *Science,* **1992**, *258*, 1122-1126.
46 L. A. Zwelling, T. Anderson, K. W. Kohn, *Cancer Res.,* **1979**, *39*, 365-369.
47 J.P. Menetski, S.C. Kowalczykowski, *J. Mol. Biol.* **1985**, *181*, 281-295.
48 H. Chao, W.-J. Mei, Q.-W. Huang and L.-N. Ji, *J. Inorg. Biochem.,* **2002**, *92*, 165-170.
49 K. Wang, J. Ruan, H. Song, J. Zhang, Y. Wo, S. Guo, S., D. Cui, *Nanoscale Res. Lett.,* **2011**, *6*, 1–8.
50 E. L. K. Chng, C. K. Chua, M. Pumera, *Nanoscale*, **2014**, *6*, 10792-10797.
51 K. Erickson, R. Erni ,Z. Lee ,N. Alem , W. Gannett, A. Zettl, *Adv. Mater.*, **2010**, *22*, 4467–4472.
52 D. R. Dreyer, S. Park, C. W. Bielawski, R. S. Ruoff, *Chem. Soc. Rev.*, **2010**, *39*, 228–240.
53 T. Szabo, O. Berkesi, P. Forgo, K. Josepovits, Y. Sanakis, Petridis, I. Dekany, *Chem. Mater.*, **2006**, *18*, 2740-2749.
54 W. Gao, L. B. Alemany, L. Ci, P. M. Ajayan, *Nat. Chem.*, **2009**, *1*, 403-408.
55 L. Wu, L. Zeng, X. Jiang, *J. A. Chem. Soc.,***2015**, *137*, 10052-10055.
56 S. R.-V. Castrillón, F. Perreault, A. Fonseca de Faria, M. Elimelech, *Environ. Sci. Technol. Lett.*, **2015**, *2*, 112–117.
57 F. Perreault, A. Fonseca de Faria, S. Nejati, M. Elimelech, *ACS Nano*, **2015**, *9*, 7226–7236.
58 R. Zhou, H. Gao, *WIREs Nanomed. Nanobiotechnol.,* **2014**, *6*, 452-474. doi: 10.1002/wnan.1277.
59 S. Liu, T. H. Zeng, M. Hofmann, E. Burcombe, J. Wei, R. Jiang, J. Kong, Y. Chen, *ACS Nano*, **2011**, *5*, 6971–6980.
60 Q. Wu, Y. Zhao, J. Fang, D. Wang, *Nanoscale*, **2014**, *6*, 5894-5906.
61 (a) Q. Wu, L. Yin, X. Li, M. Tang, T. Zhang, D. Wang, *Nanoscale*, **2013**, *5*, 9934-9943. (b) Q. Wu, Y. Zhao, G. Zhao, D. Wang, *Nanomedicine*, **2014**, *10*, 1401-1410.
62 W. Hu, C. Peng , Lv M, X. Li, Y. Zhang, N. Chen, C. Fan, Q. Huang, *ACS Nano*, **2011**, *5*, 3693–3700.
63 L. Staudenmaier. Verfahren zur Darstellung der Graphitsäure, *Ber. Dtsch. Chem. Ges.,* **1898**, *31*, 1481-1487.
64 E. L. Evans, J. de D. Lopez-Gonzalez, A. Martin-Rodriguez, F. Rodriguez-Reinoso, *Carbon,* **1975**, *13*, 461-464.
65 Y. Zhao, D. G. Truhlar, *Theor. Chem. Acc.,* **2008**, *120*, 215-241.
66 *Spartan 14*, Wavefunction Inc., 18401 Von Karman Avenue, Suite 370, Irvine, CA 92612, USA.
67 V.H. DuVernay, J.A. Pachter and S.T. Crooke, *Cancer Research*, **1980**, *40*, 387-394.